HHS Public Access

Author manuscript

J Neural Eng. Author manuscript; available in PMC 2022 June 17.

Published in final edited form as:

J Neural Eng. ; 18(4): . doi:10.1088/1741-2552/ac02dc.

Flexible, high-resolution thin-film electrodes for human and animal neural research

Chia-Han Chiang[1,15], **Charles Wang**[1,15], **Katrina Barth**[1], **Shervin Rahimpour**[2], **Michael Trumpis**[1], **Suseendrakumar Duraivel**[1], **Iakov Rachinskiy**[1], **Agrita Dubey**[3], **Katie E Wingel**[3], **Megan Wong**[1], **Nicholas S Witham**[4,5], **Thomas Odell**[5], **Virginia Woods**[1], **Brinnae Bent**[1], **Werner Doyle**[6], **Daniel Friedman**[7], **Eckardt Bihler**[8], **Christopher F Reiche**[4], **Derek G Southwell**[2], **Michael M Haglund**[2], **Allan H Friedman**[2], **Shivanand P Lad**[2], **Sasha Devore**[7], **Orrin Devinsky**[6,7,9], **Florian Solzbacher**[4,5,10], **Bijan Pesaran**[3,7], **Gregory Cogan**[2,12,13,14,*], **Jonathan Viventi**[1,2,11,14,*]

[1]Department of Biomedical Engineering, Duke University, Durham, NC, United States of America

[2]Department of Neurosurgery, Duke School of Medicine, Durham, NC, United States of America

[3]Center for Neural Science, New York University, NY, NY, United States of America

[4]Department of Electrical and Computer Engineering, University of Utah, Salt Lake City, UT, United States of America

[5]Department of Biomedical Engineering, University of Utah, Salt Lake City, UT, United States of America

[6]Department of Neurosurgery, NYU Langone Medical Center, New York City, NY, United States of America

[7]Department of Neurology, NYU Grossman School of Medicine, NY, NY, United States of America

[8]DYCONEX AG, Bassersdorf, Switzerland

[9]Comprehensive Epilepsy Center, NYU Langone Health, NY, NY, United States of America

[10]Department of Materials Science & Engineering, University of Utah, Salt Lake City, UT, United States of America

[11]Department of Neurobiology, Duke School of Medicine, Durham, NC, United States of America

[12]Department of Psychology and Neuroscience, Duke University, Durham, NC, United States of America

[*]Authors to whom any correspondence should be addressed. j.viventi@duke.edu**and** gregory.cogan@duke.edu.

Author contribution: CHC, CW, KB, and JV designed and tested the electrode setup and custom hardware. MW, VW, and BB performed initial development and pilot experiments. CHC and IR fabricated SEEG prototype devices in the cleanroom. EB provided the LCP electrode cross-section photo and early material biocompatibility data. NSW, TO, CFR, and FS performed array flexibility evaluation. AD, KEW, and BP performed stimulation testing. CHC, MT, SD, KB, GC, and JV analyzed and interpreted the data. CHC, KB, SR, SD, BP, GC, and JV collected data. SR, WD, DF, DGS, MMH, AHF, SPL, SD, OD consulted for electrode design and deployment system, and performed surgery. CHC, CW, and JV wrote the initial manuscript. GC and JV secured funds for this project.

Data availability statement

The data generated and/or analysed during the current study are not publicly available for legal/ethical reasons but are available from the corresponding author on reasonable request.

Supplementary material for this article is available http://doi.org/10.1088/1741-2552/ac02dc

[13]Center for Cognitive Neuroscience, Duke University, Durham, NC, United States of America

[14]Duke Comprehensive Epilepsy Center, Duke School of Medicine, Durham, NC, United States of America

[15]These authors contributed equally to this work.

Abstract

Objective.—Brain functions such as perception, motor control, learning, and memory arise from the coordinated activity of neuronal assemblies distributed across multiple brain regions. While major progress has been made in understanding the function of individual neurons, circuit interactions remain poorly understood. A fundamental obstacle to deciphering circuit interactions is the limited availability of research tools to observe and manipulate the activity of large, distributed neuronal populations in humans. Here we describe the development, validation, and dissemination of flexible, high-resolution, thin-film (TF) electrodes for recording neural activity in animals and humans.

Approach.—We leveraged standard flexible printed-circuit manufacturing processes to build high-resolution TF electrode arrays. We used biocompatible materials to form the substrate (liquid crystal polymer; LCP), metals (Au, PtIr, and Pd), molding (medical-grade silicone), and 3D-printed housing (nylon). We designed a custom, miniaturized, digitizing headstage to reduce the number of cables required to connect to the acquisition system and reduce the distance between the electrodes and the amplifiers. A custom mechanical system enabled the electrodes and headstages to be pre-assembled prior to sterilization, minimizing the setup time required in the operating room. PtIr electrode coatings lowered impedance and enabled stimulation. High-volume, commercial manufacturing enables cost-effective production of LCP-TF electrodes in large quantities.

Main Results.—Our LCP-TF arrays achieve 25× higher electrode density, 20× higher channel count, and 11× reduced stiffness than conventional clinical electrodes. We validated our LCP-TF electrodes in multiple human intraoperative recording sessions and have disseminated this technology to >10 research groups. Using these arrays, we have observed high-frequency neural activity with sub-millimeter resolution.

Significance.—Our LCP-TF electrodes will advance human neuroscience research and improve clinical care by enabling broad access to transformative, high-resolution electrode arrays.

Keywords

intraoperative; ECoG; electrode; iEEG; LCP; Brain Machine Interface (BMI); Neural Interface

1. Introduction

The brain is a complex control center that processes and responds to sensory inputs and coordinates a range of functions from physiological (muscles and organs) to psychological (mood and thoughts). These operations involve organized activity of large neuronal populations across multiple brain regions. To record brain activity with large spatial coverage, intracranial electroencephalography (iEEG), or electrocorticography (ECoG), is

commonly used. ECoG utilizes a soft and flexible array of metal disc electrodes to sense neural activity (local field potential, LFP) from the surface of the cortex. Although ECoG is mainly used to plan epilepsy surgeries, it can reliably record signals over years after implantation [1], which makes it also a promising interface for chronically implantable neural prostheses [2].

Advances in microfabrication techniques have created electrode arrays with sub-millimeter resolution [3–6]. These micro-fabricated ECoG arrays (micro-ECoG, or μECoG) can measure rich microscale neural-dynamics that were previously undetectable by coarsely sampled (centimeter scale) clinical grids (CG). For example, fine-scale spatial temporal patterns emerge in an induced seizure model when sampled with sub-mm resolution [7]. Furthermore, with increases in spatial resolution, action potentials can be recorded from the cortical surface [8]. Therefore, reducing electrode-site size and increasing electrode density enables sensing of signals from the cortex that are undetectable with standard CGs.

For clinical applications in epilepsy patients, high density electrodes can improve diagnostic efficacy by better defining the epileptogenic cortex [9]. Standard CGs, which contain macroelectrodes alone (2.3 mm diameter, 10 mm spacing), sparsely sample epileptiform tissue and lack the signal resolution necessary to resolve focal neuronal sources. Microelectrode arrays for seizure diagnostics offer higher spatial resolution [10, 11], improved seizure detection rates [12], and may identify precursors that predict clinical seizures [12, 13]. For instance, microscale electrode arrays can better detect high-frequency broadband neural activity which has been shown to have high correlation with multi-unit spiking activity [14], high-frequency oscillations (HFOs) [15–17] and microseizures[13, 18, 19] that are missed or poorly sampled with CG electrodes. Microseizures can be detected more than one minute earlier than the signals recorded with typical CGs [13]. Enabling broad access to microelectrodes would allow the measurement of microseizures to become part of routine clinical care and could improve seizure warning systems [20, 21].

The potential for microscale signals to better inform seizure diagnostics, as well as research on cognition [22] and brain-machine interfaces [5, 23–26], has motivated several electrode manufacturers to integrate protruding microwires into clinical macroelectrode grids. Several of these devices have FDA approval but technical challenges limit their widespread adoption. Commercial microwire grids have very high and varying impedances (<100 kΩ to 6–8 MΩ), owing to their non-uniform exposure from the insulating substrate. Additionally, their ‘sharp, ragged’ metal edges can damage the brain [27]. Recording from microelectrodes with clinical data acquisition (DAQ) systems can distort signals because microelectrodes have far higher impedances than macroelectrodes [28] and require amplifiers with higher input impedances to produce reliable, low noise recordings with minimal crosstalk [29]. Finally, microwire hybrid grids typically only have a small number of microwire electrodes (~16) and limited coverage due to limitations in the clinical connector design [13, 30, 31]. Therefore, although microelectrodes have been introduced into clinical applications, their integration remains limited.

To meet the need for high-resolution neural interfaces that could enhance scientific discovery and advance clinical therapies, we have developed, extensively tested, and

successfully recorded from novel electrode arrays based on thin-film (TF) technology using liquid crystal polymer (LCP) manufactured by our medical device manufacturing partner Dyconex AG. In previous studies, we developed a 61ch array and tested its chronic reliability for over 1 year in rats [32]. We have also developed a 244ch array for use in non-human primates (NHP), with the capability to simultaneously record from individually movable, penetrating microelectrodes [33]. In this paper, we demonstrate improvements on these prior results by translating LCP-TF electrodes to human intraoperative research, including electroplating electrode contacts with platinum iridium (PtIr) to enable stimulation. We provide demonstrations of intraoperative recordings that highlight the focal information that can be captured with LCP-TF electrodes that may be missed with CGs. We also developed a complete electrical and mechanical recording setup to facilitate efficient intraoperative research and rapid dissemination of LCP-TF electrodes to interested researchers. Our advances in electrode manufacturing, design, and implementation will enable high-channel count, micro-scale human neuroscience research.

2. Material and methods

2.1. Electrode

We have designed five LCP-TF electrodes for different applications (figure 1) ranging from rodents to humans. High-resolution electrodes typically require expensive semiconductor micro-fabrication techniques in a cleanroom environment, which makes large scale production and wide dissemination challenging. We leveraged flexible printed circuit (FPC) technology to inexpensively manufacture a large quantity of LCP-TF electrodes. All electrodes shown in figure 1 were fabricated with our medical device manufacturing partner, Dyconex, AG (CH).

2.1.1. LCP material—Fabricating electrodes using LCP offers many advantages. LCP is long-lasting, with water permeability ~25× lower than commonly used FPC materials such as polyimide [34], which dramatically extends implanted array reliability and lifetime. LCP is also a self-adhering thermoplastic material, which requires no additional adhesives or glues when combining multiple sheets. Accelerated aging studies project that the devices would maintain their electrical performance for at least 5 years when implanted [32]. By contrast, polyimide electrode arrays rely on interlayer adhesion and can delaminate in <1 year [32].

In addition, LCP has a higher working temperature than typical printed circuit board (PCB) material (FR-4) style laminates, good high frequency properties, high chemical resistance, and strong barrier properties [35]. This higher working temperature, combined with monolithic fusing of the LCP layers, allows our hybrid chronic implant design (80ch) to be sterilized using autoclaving. All of the LCP-TF electrodes can also be sterilized by ethylene oxide (EtO) or vaporized hydrogen peroxide sterilization (VHP).

2.1.2. Array design—The LCP-TF electrodes were fabricated with a minimal 2-metal layer design, where the electrode contacts were almost flush or slightly protruded from the LCP substrate to ensure good contact to brain tissue (figures 2(A) and (B)), rather than opening the top layer and having the electrode contacts recessed down in a well. Dyconex

used conventional flexible PCB technologies and related equipment to fabricate these arrays. The fabrication steps started with the dual sided copper clad LCP sheet (Ultralam HT 3850, Rogers Corp.). The copper on the LCP sheet was etched off before applying the photoresist. Photolithography was performed to pattern the electrodes on the top layer and the wires on the bottom layer. Vias were laser-drilled to connect the electrodes to the wires on the bottom side. A thin palladium (Pd) seed layer was deposited and the resist structure was lifted from the substrate. Gold was electroplated on top of the Pd structures to the desired thickness. All processes were done on both sides of the LCP substrates simultaneously.

For improved flexibility, we used two of the thinnest LCP sheets commercially available (25 μm each). With heat (>280 °C) and pressure (>300 psi), a blank LCP sheet (Ultralam 3908, Rogers Corp.) was laminated to the bottom side of the substrate to encapsulate all of the wiring. Through this lamination process, the two LCP sheets were monolithically fused into a single layer, with gold (Au) wiring encapsulated in between (figure 2(C)). The interfaces between the LCP layers were not visible after fusing, preventing water ingress into the device from the edges, which is a common cause of delamination in polyimide devices, and a leading cause of device failure [36]. After fabrication, the total LCP-TF electrode thickness was just over 50 μm.

Only metals that are considered biocompatible (Au, PtIr and trace Pd) [37, 38] were used in the LCP-TF devices. *In vitro* tests showed LCP-TF electrodes meet biocompatibility criteria guided by ISO 10993–5 [39]. Implanting similar LCP-TF electrodes in rabbit retina for 2.5 years showed no adverse effects [34]. LCP-TF electrodes produced by Dyconex have successfully passed ISO 10993–5 [40].

The LCP-TF electrodes include much thicker (5 μm) Au layers than traditional TF devices (~0.1 μm). This reduces the resistance of the wires and improves their durability to surgical handling. A different LCP device design with thinner Au wires (500 nm) was bend tested to a 1 mm bend radius (nearly folding) and achieved 6000–12 000 bend cycles before failure [38]. The wire widths and spacings used ranged from 30/30 μm to 60/40 μm, respectively. The finer design (30/30 μm) was used where high density was required and wider wires and spacing (60/40 μm) were used wherever possible to minimize trace resistance and increase fabrication yield. The wire resistance for a 60 μm wide wire was ~7 $\Omega\ cm^{-1}$.

Our microelectrode impedance was much lower and more uniform than microwire arrays [27] due to larger surface area (200 μm vs 40 μm dia.) and precise lithographic patterning of the electrode contacts. All electrode contacts were fabricated with gold as the base metal. Some arrays were electroplated with PtIr (Platinum Group Coating LLC), to reduce the electrode impedance [41, 42]. This electrodeposited PtIr coating has demonstrated lower impedance, decreased noise, and increased signal-to-noise ratio (SNR) in chronic implants [43]. Immunohistochemistry showed no significant differences in the immune response between PtIr coated and uncoated electrodes [43]. The PtIr coating was applied at room temperature, making it easy to integrate with standard FPC manufacturing processes, a crucial design consideration for large-scale manufacturing.

We designed the LCP-TF electrodes so that no additional soldering or assembly was required to connect the electrodes with recording headstages. This substantially reduced the difficulty and cost of manufacturing. We used a FPC zero-insertion-force (ZIF, FH43B, Hirose Inc.) connector and an ultra-low profile, high-density (0.8 mm pitch) spring connector (ZA8, Samtec Inc.) (figure 3). The ZA8 is highly reliable and has demonstrated 100% connection yield and low resistance after 1000 connection cycles [44]. Both connectors only required a specified thickness of stiffening material added to the bottom of the connector region. Using standard high-density FPC connectors reduced the amount of post-processing required for the LCP-TF arrays.

2.2. Molding

For LCP-TF electrodes used in human intraoperative research, we have molded the electrode in medical grade silicone (MDX4–4210, Dow Corning) to provide soft, rounded edges [33, 45, 46], reducing the possibility of the thin LCP edges damaging the cortex during surgical placement. The molded device was ~200 μm thick, <30% of the thickness of CG electrodes (AdTech, 850 μm). The silicone molding was also used to combine multiple LCP-TF electrodes, creating a single array with larger coverage and uniform contact spacing (supplement figure 1 (available online at stacks.iop.org/JNE/18/045009/mmedia)). We have used similar molding methods for NHP implants in prior studies [33, 47]. Additionally, the silicone molding can provide mechanical features, such as bending the cable arm to 90° to facilitate electrode placement during intraoperative recordings.

2.2.1. Array molding—The general array molding steps are shown in figure 4(A). We used water-soluble tape (5414, 3 M) to temporarily protect the electrode contacts during molding. A medical-grade silicone primer (MED1–161, Nusil) was used to strengthen the bond between the LCP-TF and the silicone. A stainless-steel stencil, pre-treated with medical-grade demolding agent (MCC-DGF14 A, MicroCare Corp.) was used to control the shape and thickness of the silicone molding. Samples were heated to 60 °C to reduce the silicone curing time to 2 h. Finally, molded arrays were released by rinsing with warm (>40 °C) deionized (DI) water. This molding method achieved a nearly flush boundary between silicone and LCP at the device edges (figure 4(B)), yielding a flexible array that had a much flatter surface topography compared to CG electrodes (figure 4(C)). The electrode contacts were also nearly flush with the surface (figure 4(C)). In contrast, CG electrode contacts are recessed from the surface of the array by ~200 μm, potentially causing irritation to the brain from the unevenness of the surface features.

2.2.2. Forming the coiled leads—For the chronic array, the flat LCP-TF ribbon cabling, which carries micro-wiring from contacts to connector, must be converted to a round, flexible lead for proper tunneling and suturing during semi-chronic implantation. We achieved this by winding the LCP-TF ribbons around a 1.6 mm diameter steel core to form a coiled shape and then inserting the coil into a 2.8 mm outer diameter polyurethane tube (Nordson Medical). The metal winding core was removed, and the tube was filled with silicone to ensure that no empty space was left inside while keeping the lead round and flexible.

2.3. Array flexibility evaluation

To assess the maximum bending force that could be exerted on the brain by the electrodes, we conducted four-point flexural bending tests on LCP-TF and CG arrays. To account for any anisotropy, this bending test was done at three angles (0°, 45°, and 90°) on the horizontal plane of each array. These tests were repeated 12 times per array. With force and displacement data, we calculated the effective flexural modulus. This modulus was then used to determine the maximum force that an electrode array could exert on the brain. This was calculated assuming the array would have to bend to a radius of 60 mm, which was the smallest radius of curvature of an MRI brain scan obtained from the NIH 3D Print Exchange (Model 3DPX-000320). The mean maximum force values of each array were averaged across all angles and the standard deviation between the means of each angle were obtained. These results were then used to calculate the standard error of means for each sample. This was done to demonstrate both the average maximum force for each array and the range of maximum force each array could exert. We used this method to compare an FDA-approved commercially available ECoG electrode array (Ad-Tech Medical Instrument Corporation, FG64C-SP10X-000) and an LCP-TF device prototype without Au traces. More details about the testing setup and procedure as well as a more detailed analysis of these and other relevant material samples can be found in another study [48].

We compared the stiffness of the molded chronic array mechanical prototype (200 μm thick total, no Au wires) to an FDA-approved, conventional ECoG electrode array (Ad-Tech) through a four-point flexural bending test setup. The LCP-TF prototype device was ~11× less stiff than the commercial ECoG array. The mean and SEM force for the LCP-TF prototype device was 6 ± 1 mN, while the commercial ECoG array force was 67 ± 17 mN (figure 4(D)).

2.4. Data acquisition system

Long wires between microelectrodes and the recording system can cause signal distortions and increased noise [27]. Commercially available headstages amplify and digitize 32–64 channels simultaneously but are not designed to scale up to record hundreds or thousands of channels. Therefore, we have designed a modular adapter system with a miniature digitizing headstage using a 64-channel digital electrophysiology integrated circuit (RHD 2164, Intan Technologies LLC). Our 64-channel digitizing headstage was compact, 19 × 20 mm, and weighed 2.0 grams (figure 5(A)). The small size and light weight of the digitizing headstage made it suitable for use in freely behaving rat experiments as well as larger animals and humans. The digitizing headstage was connected to different modular adapter boards, which were designed to minimize the physical footprint and enable daisy chaining multiple headstages together to reduce the number of connections required during intraoperative experiments (figure 5(B)). We used standard micro-HDMI cables to enhance reliability and accessibility. For the back-end acquisition system, we modified the Intan 1024ch controller (C3008, Intan Technology) to be powered with an external DC battery to reduce power line noise (60 Hz) and to eliminate any connection to AC power for additional electrical safety (supplement figure 2). The 1024ch controller additionally includes galvanic isolation of the power and data lines for each headstage port. The complete DAQ system was approved

by the Duke University Hospital Clinical Engineering and NYU Langone Hospital Clinical Engineering departments.

2.5. Stimulation experiment

Three 61ch LCP-TF arrays with PtIr electrode coatings were evaluated for electrical stimulation. The arrays were tested *in vitro* in 0.9% saline. We used a multichannel recording and stimulation system to deliver stimulation and measure electrode impedance (RHS 128-channel stimulation/recording controller system and RHS 32-channel headstage, IntanTechnology). One million biphasic current pulses (124 μA, 200μs per phase, cathode first, 40 Hz repetition rate) were applied to four selected channels on each 61ch array. A total of 12 channels were tested. The initial and final impedance measurements were taken at nine different frequencies of 75, 100, 200, 400, 500, 800, 1000, 2000, and 4000 Hz.

2.6. Intraoperative experiments

We have recorded from multiple participants using our high-density, molded, LCP-TF electrode arrays placed subdurally over the surface of the brain for up to 30 min during epilepsy surgery, brain tumor resection, or deep brain stimulator (DBS) placement. Participants gave their written informed consent before the day of the surgery. All participants were fluent in English. All protocols were approved by the Duke Health and NYU Langone Institutional Review Board. All experiments and data in this study complied with all relevant ethical regulations. Electrodes with holders were sterilized with EtO at Duke Hospital or VHP at NYU Langone Hospital.

In this paper, we report the data from two participants. One participant, a 20 year-old female, heard a series of words and non-words during an asleep craniotomy for seizure focus resection. μECoG signals were recorded using a 244ch array placed over the posterior superior temporal gyrus (pSTG), while the participant passively listened to 336 words and non-words (randomized into four blocks of 84 trials). Data were acquired at a sampling rate of 20 000 samples per second (SPS).

The other participant, a 42 year-old male, performed a directed finger movement task during an awake craniotomy for brain tumor resection. The participant wore a 5DT Data Glove (Fifth Dimension Technologies, Orlando FL), used to record finger kinematics, on the contralateral hand, while performing the task. The μECoG signals were recorded by a 244ch array over the 'hand-knob' region of the motor cortex. A presentation laptop was used to cue the patient to flex the appropriate finger repeatedly until a rest period followed by a new cue (finger). The overall experiment contained 75 trials (randomized into three blocks) with 15 trials per finger. Each trial contained up to 5 s of finger movement.

2.6.1. Recording system for open craniotomy experiments—For intraoperative recordings in epilepsy or brain tumor surgery, we utilized a modified METRx™ flexible arm (Medtronic, St. Paul, MN) to hold the 244ch LCP-TF electrode deployment system (figure 6(A)). The system was slowly lowered down for the electrode to make contact with the cortical surface (supplemental movie 1). Spring tension in the arm prevented excessive force from being transmitted to the brain. The deployment system structure was made out of

stainless steel, machined in house. The stainless steel base provided an electrical connection to bridge the reference and ground connections for each of the four digitizing headstages together (figure 6(B)). A 3D printed housing, made out of biocompatible material (Duraform PA, 3D System), protected the electronics and enabled easy handling of the system during surgery. Slot openings were included in the housing to allow sterilization gas to reach the internal components (figure 6(C)). The same design principles were used to scale to 1024 channels (figures 6(D) and (E)). We have successfully used this open-craniotomy intraoperative recording setup 21 times.

2.6.2. Recording system for DBS experiments—To record from the cortex in patients undergoing DBS surgery, we made a flexible, long, and narrow LCP-TF electrode (128ch). The LCP-TF electrode was inserted through a small, 14 mm diameter burr-hole and advanced more than 80 mm away from the burr-hole site along the cortical surface (figures 7(A) and (B)). We designed a mechanical holding structure that was integrated with NexFrame stereotactic system (Medtronic, St. Paul, MN) (figure 7(C)). The system is also adaptable to other methods of DBS implantation (e.g. frame based stereotaxy). The tip of the LCP-TF electrode was also molded with an extra silicone pocket to temporarily hold a malleable brain retractor device (R8960, T. Fukushima Brain Spatulas, Integra) to facilitate subdural array tunneling and navigation (figure 7(D)). The 128ch LCP-TF electrode included a ruler on the back side of the array to assist in targeting when sliding under the dura (figure 7(E)). The ruler was printed with a biocompatible solder mask (NPR-80, Nippon Polytech Corp.). Electrode placement was verified during intraoperative computerized tomography acquisition which was used to confirm DBS lead placement. Up to the day of submission, we have deployed this array design four times intraoperatively during DBS surgeries.

2.7. Data analysis

In both auditory and motor experiments, the recordings from each channel were subjected to common-average-referencing to remove line noise. We rejected electrode channels from the common average with high impedance (>1 MΩ). To display data spatially, we predicted noiseless neural potential fields using Gaussian process modeling of the electrode recordings [49]. To adapt to time-varying spatial statistics, spatial covariance kernels were updated at latent state transitions, which were estimated by hidden Markov modeling of the average signal power envelope.

2.7.1. Spectrogram analysis—To examine spectral features in each electrode, we computed spectrograms for each channel. We decomposed the data into time-frequency components using a multi-taper spectral analysis with a 500 ms analysis window (50 ms time steps) and 10 Hz frequency smoothing [50]. We then normalized the spectrograms by computing the average $1/f$ spectral estimate during the baseline period (−0.5–0 s before auditory onset) across all trials and dividing the spectral time steps by the mean estimate for each frequency band.

2.7.2. High gamma extraction and electrode significance—We used the high-gamma (HG: 70–150 Hz) band to characterize the neural response from our LCP-TF

electrode, as it has shown to be a local index of cognition and a strong correlate of multi-unit firing [51–53]. From previously established methods, we used IIR filters to filter data into eight frequency bands between 70 and 150 Hz [54]. We computed the envelope of each band using the Hilbert transform and then averaged the resultant envelopes across all bands to create a total envelope. Finally, we down sampled the filtered HG band to 200 Hz and normalized (z-scored) the envelope from the baseline responses (−0.5–0 s post stimulus onset) across all trials.

To assess electrode significance, we computed the average HG power (unnormalized) across trials in two time regions ('baseline' and 'response') of interests for each trial. For the auditory experiment, we defined 'baseline' as the 500 ms time window prior to auditory onset and 'response' as the time window from 250 to 750 ms post onset. For the finger flexion tasks, 'baseline' was defined as the 500 ms window prior to stimulus onset during which no finger movement was observed, and 'response' was defined as −250–250 ms centered around flexion onset. We identified statistically significant channels by comparing the power between baseline and response using a 10000 iteration one-sided empirical permutation test [55]. We corrected the significance across electrodes to an alpha level of 0.05 with the false discovery rate procedure [56] (one—sided FDR corrected, $P < 0.05$).

2.7.3. Linear decoder for finger flexion analysis—We used a previously established linear classification scheme to decode finger stimulus conditions from HG responses [57, 58]. Normalized HG time-segments (length T) during response conditions were concatenated from significant channels (S sites) as feature vectors (length—ST) for each finger trial. The ST feature vectors were *z*-score normalized and compressed using singular value decomposition (SVD) with leave-one-out cross-validation. Finally, the singular scores from the compressed training-set were used to build a supervised linear discriminant (LD) model to decode finger conditions. To validate the model, the ST features of the test-set were compressed using the trained-SVD model and the corresponding scores were used to predict finger flexions using the supervised LD model. The optimal number of SVD components were obtained using nested cross-validation for each training-test set and the overall accuracy was estimated from the percentage of total correct predictions. We trained two different models: one to decode five-fingers (five-way) and another for three-finger (three-way, thumb, index, and little) movements.

3. Results

3.1. Stimulation capability

The electrode contacts were electroplated with PtIr. PtIr coatings are highly fractal and exhibit pseudocapacitive reactions, dramatically increasing the electrode surface area [41, 42] (figure 8(A)), and thus decreasing contact impedance by an order of magnitude, from 44 ± 13.9 kΩ to 4.6 ± 1.8 kΩ at 1 kHz (figure 8(B)). This lower impedance provided an improved SNR [43] and enabled stimulation. A total of 12 channels in three arrays were tested with one million biphasic current pulses (124 μA, 200 μs per phase, cathode first, 40 Hz repetition rate). PtIr coated electrodes showed no degradation after one million pulses at twice the clinical neural stimulation safety limit (30 μC cm^{-2}) [59] (figure

8(C)). We further tested the maximum current limit placed through the electrodes without causing damage. The maximum current we arrived at without overshooting the compliance limit setting was 1.275 mA (200 μs per phase, cathode first, 40 Hz repetition rate). The microelectrodes showed no sign of degradation after one million pulses at 1.275 mA as well. The impedances, at 1 kHz, of the contacts before and after one million pulses at 1.275 mA were 6.6 ± 1.3 kΩ and 5.8 ± 0.7 kΩ (N = 6), respectively. Although the clinical safety limit for microelectrode stimulation is still undecided, this higher stimulation current is still below the Shannon limit (k = 1.85) [59] and has been used in animal research [60, 61].

3.2. High resolution recording

We report the data from two participants demonstrating the utility of high-resolution recording. In the first case, we used our 244ch LCP-TF array to record neural responses from the pSTG of an anesthetized patient by presenting an auditory stimulus (figure 9(A)). Uniform *in vivo* impedance measurement was observed in this experiment (supplement figure 3). We removed noisy single trials for each channel by identifying trials with absolute voltage amplitudes that exceed ten times the standard deviation. Spectral analysis of the recordings demonstrated an increase in the power of high gamma band (75–150 Hz) neural signals during auditory onset (figure 9(B)). The plotted area contains 244 channels, covering a total area of 12 × 12 mm^2, and each electrode demonstrates a different neural response profile in the HG band. We examined the significance of our μECoG channels by comparing the HG power from auditory onset with respect to baseline. The one-sided permutation test identified 108 channels (out of 244, $p < 0.05$) with significant HG power and revealed a spatial pattern within the 16 × 16 grid (figure 9(C)). Further, our 244ch array showed a clear spatiotemporal progression of auditory processing at high resolution in pSTG (figure 9(D)). This spatio-temporal activation pattern occurred over a total of area of less than 12 × 12 mm^2, indicating a pattern that would only be detectable by μECoG as contacts on standard CG arrays are too large (2.3 mm diameter) and spaced too far apart (10 mm) to detect neural activation patterns at this spatial scale.

In the second case, we recorded motor neural responses using a similar 244ch LCP-TF array from the ‘hand-knob’ area in the motor cortex during a finger movement task (figure 10(A)). The finger kinematics were recorded using a data glove (figure 10(B)). Although this array contained some higher impedance channels (supplement figure 4), we found clear motor responses in the high-gamma band that had a spatial organization (figure 10(C)). Our statistical analysis identified 24 channels with significant HG power, mostly grouped at the top-right corner of the array (figure 10(D)) and were used in the decoding analysis. Normalized HG responses revealed finger related activity indicating a clear, distinctive spatial-temporal organization of motor processing, with respect to the five fingers, within the 8 × 8 grid (figure 10(E)). The top right corner also appeared to react most strongly when the thumb was instructed to move. To demonstrate the decoding potential of our array, we used the HG responses from the above 24 sites to classify finger movements using a linear discriminant classifier, as described in section 2. In the five-finger decoding, the classifier was successful in identifying the finger types with an average decoding accuracy of 61% (chance 20%), with maximum decoding accuracies for the thumb. Further analysis indicated that the increased classification error between middle, ring, and little finger, were caused by

natural co-contraction [62], where multiple fingers move together when only a single finger was instructed to move. These natural co-contractions were confirmed by increased glove kinematic correlations between the middle, ring, and little finger (supplementary figure 5). To examine flexion analysis between independent finger articulations, we then reduced the analysis to a three-way decoder to classify between thumb, index, and little finger, which yielded an average decoding accuracy of 96% (chance 33.33%) (figure 10(F)). This nearly perfect decoding was achieved in a predominantly thumb responsive area of cortex. These 244ch array intraoperative recordings demonstrate the ability of our LCP-TF arrays to record and decode auditory and motor information at high resolution.

3.3. Chronic array

We have designed high-resolution electrodes for epilepsy pre-surgical evaluation. This LCP-TF design is intended for semi-chronic implants up to 30 d. For clinical use, it is important to maintain the clinical standard macro-electrodes, in addition to the micro-electrodes. Further, the electrode cables must be passed through a standard cannula (3 mm dia.). Round cables are preferred to allow surgeons to suture and seal the dura and scalp around the cables (see section 2.2.2).

Here we show an LCP-TF design which meets these criteria (figures 11(A) and (B)). We have designed an 80ch hybrid LCP-TF array with 76 research micro-electrodes interspersed amongst four macro-electrodes of clinical-standard size and spacing. While other TF electrodes use flat ribbon cables that cannot be implanted by standard surgical procedures, our LCP-TF array has rounded leads that neurosurgeons consider acceptable for short-term (<30 d) implantation. The planar TF-LCP cables are molded into helically wound leads of 2.8 mm diameter without sharp edges to allow longitudinal elongation (up to 15%) (figure 11(C) and section 2.2.2). These leads are similar to existing CG electrode leads and can be tunneled through the skin as in current surgeries but contain 5–10× more channels than traditional CG electrode leads. In addition, when combining multiple arrays to a 4 × 4 cm coverage, we have developed a novel, high-density connector system where all percutaneous leads will be inserted into a custom lead carrier that provides easy placement and guaranteed alignment with the ZA8 spring connectors (described in section 2) (figures 11(D) and (E)).

4. Discussion

We have successfully demonstrated the ability to record from LCP-TF electrodes in rodents, NHPs, and humans. This has been accomplished through advances in design, fabrication, and implementation. In the current work, we demonstrate this ability in human recordings from two participants performing a passive listening task and a finger movement task. Micro-scale spatio-temporal neural activation patterns were shown in both the auditory (pSTG) and motor (hand motor cortex) brain regions.

While these results of our initial experiments in rodents, NHPs and humans are promising, much work remains to be done. This includes (a) developing LCP-TF electrodes to record from deep brain structures, (b) further increasing the spatial resolution of the electrodes, (c) performing required safety and biocompatibility studies for FDA 510(k) approval, and

(d) exploring applications of LCP-TF electrodes to cognitive, motor, visual, and auditory prostheses.

Recently, stereo-electroencephalographic (SEEG) electrodes have been increasingly adopted for seizure monitoring. The resurgence of SEEG compared to ECoG is largely attributable to the reduced inflammation, infection and pain using robotic minimally invasive surgical techniques [63]. Our LCP-TF technology could be applied to SEEG as well. As a proof of concept, we have developed a 61ch LCP-TF SEEG electrode that included both micro- and macroelectrodes, similar to other efforts [64]. Our LCP-TF SEEG electrode was rolled and molded into a cylindrical shape only ~900 μm in diameter (figure 12), the same form factor as clinical-standard SEEG arrays. Our LCP-TF SEEG electrode could be used to record from deep brain structures as well as cortical structures, though more testing and validation of this design is required. Future work will focus on demonstrating the functionality, safety, and efficacy of the LCP-TF SEEG design.

We have recently determined that sub-millimeter electrode density is required to reliably sample neural activity in multiple species including human [49]. Using spatial analysis (‘kriging’ [65]), we established the effect of sampling density on interpolation error, and determined the kriging resolution required for <10% interpolation error in 95% of cases [49]. The required spacing varied across species, and across temporal bandpass. In a noise-free setting, the spacing needed to sample high frequency activity (75–300 Hz) in human auditory cortex under anesthesia was 622 μm. While our initial LCP-TF electrodes have a range of 0.42–2 mm spacing, this result indicates that further increases in sampling density will likely be required. However, the LCP-TF arrays described here provide an important step towards high-resolution neural interfaces before the next generation of electrodes with embedded flexible electronics [66–68] are fully tested and available for clinical use.

Our LCP-TF recordings and other microelectrode recordings over the past 10 years [10–13, 15–19] have revealed a striking heterogeneity in the spatiotemporal dynamics of interictal epileptic events including HFOs, interictal discharges, and microseizures. However, all of these studies have been limited by their inability to observe microscale dynamics of human epileptic cortex simultaneously at high resolution and with large cortical coverage. To further relate these high-resolution electrophysiological events to clinical events like seizure initiation, propagation, and termination, researchers need to be able to implant our LCP-TF electrodes over the putative seizure onset zone and then obtain continuous recordings in the epilepsy monitoring unit. Such a clinical study is not possible without FDA approval of the electrodes. Our LCP-TF electrode design contains conventional macroelectrodes for clinical care and microelectrodes for research. Our next step will be to perform the required biocompatibility and safety studies to obtain FDA 510(k) clearance for short-term (<30 d) implantation.

A critical advantage of our LCP-TF electrodes over existing technologies is their low cost compared with standard clinical electrode arrays. The LCP-TF electrodes cost half as much per square centimeter compared to conventional clinical arrays and other alternatives. CGs typically come in 4–10 channel strip and 8–96 channel grid configurations. Typical sales prices for these devices range from $450 to $1400. We used technologies that are designed

to compete with high volume printed circuit board manufacturing. Our LCP-TF effective cost was ~$4 cm^{-2} including the lead and connector, which is often not included in cost comparisons.

Increased availability of high-resolution electrodes will facilitate the broad collection of high-resolution neural data from humans for many applications, including better informing seizure diagnostics [7, 13, 15, 69–72], improved therapies for motor disorders and enhanced prosthetic systems. We have already started disseminating the LCP-TF electrodes described in this paper to more than ten labs and will continue to make our technology available for broader investigative use. Our platform technology can be adapted for patients with sensory and motor deficits treated with penetrating microelectrodes in proof-of-concept brain-machine interfaces as well. Exploratory studies in epilepsy patients with high rates of mood and memory symptoms [73] can extend this technology to study mood and cognitive disorders.

Higher resolution electrode arrays will also enable improved motor brain-machine interfaces [5, 23–26], visual [74], auditory prostheses [23, 75–81], and enhanced research of cognition [22]. High resolution recordings will be increasingly important for the next generation of therapeutic and prosthetic neural devices [82–86]. In each case, high-resolution recording and stimulation is required. Our system will achieve these goals by increasing spatial resolution, while maintaining clinically relevant coverage, using a thinner and more efficient electrode and cabling system.

5. Conclusion

In this paper, we have developed a platform technology to enable high-resolution cortical interfacing, in a form factor that is scalable, cost effective, and compatible with current clinical care. We demonstrated LCP-TF electrodes and supporting system designs suitable for animal and human research. The LCP-TF electrodes were designed to cover a wide range of research subjects, recording densities, and spatial coverages. Silicone molding allowed us to combine multiple arrays to further extend the spatial coverage. The mechanical deployment hardware positioned the amplifier and digitizer very close to the electrodes, reducing the effect of environmental noise sources. We have already shared many of these devices for animal use and are preparing for broader dissemination to many more interested users. Dissemination of our high-resolution LCP-TF electrodes will lead to a significant acceleration of research progress and offer powerful insights into human brain activity.

Supplementary Material

Refer to Web version on PubMed Central for supplementary material.

Acknowledgments

The cartoon icons in Figure 1 are from www.biorender.com.

Grant#DoDEP200077, NIH U01 NS099697, NSF CBET-1752274, NIH CTSA grant UL1TR002553 and Find A Cure for Epilepsy and Seizures (FACES).

Competing interests: Parts of the technology described here are patent pending under 'Electroencephalography (EEG) Electrode Arrays and Related Methods of Use' U.S. Patent Application # PCT/US2020/051400. F. Solzbacher declares financial interest in Blackrock Microsystems LLC and Sentiomed, Inc, managed by University of Utah's COI management. W. Doyle and D. Friedman declare financial interest in Neuroview Technology overseen by NYU Grossman School of Medicine's COI management.

References

[1]. Bergey GK et al. 2015 Long-term treatment with responsive brain stimulation in adults with refractory partial seizures Neurology 84 810–7 [PubMed: 25616485]

[2]. Benabid AL et al. 2019 An exoskeleton controlled by an epidural wireless brain–machine interface in a tetraplegic patient: a proof-of-concept demonstration Lancet Neurol. 18 1112–22 [PubMed: 31587955]

[3]. Shokoueinejad M. et al. 2019; Progress in the field of micro-electrocorticography. Micromachines. 10 :62.

[4]. Brodnick SK. et al. 2019; μECoG recordings through a thinned skull. Front. Neurosci. 13 :1017. [PubMed: 31632232]

[5]. Slutzky MW, Jordan LR, Krieg T, Chen M, Mogul DJ and Miller LE 2010 Optimal spacing of surface electrode arrays for brain–machine interface applications J. Neural. Eng 7 26004 [PubMed: 20197598]

[6]. Welle EJ, Patel PR, Woods JE, Petrossians A, Della Valle E, Vega-Medina A, Richie JM, Cai D, Weiland JD and Chestek CA 2020 Ultra-small carbon fiber electrode recording site optimization and improved in vivo chronic recording yield J. Neural. Eng 17 26037

[7]. Viventi J et al. 2011 Flexible, foldable, actively multiplexed, high-density electrode array for mapping brain activity in vivo Nat. Neurosci 14 1599–605 [PubMed: 22081157]

[8]. Khodagholy D, Gelinas JN, Thesen T, Doyle W, Devinsky O, Malliaras GG and Buzsaki G 2014 NeuroGrid: recording action potentials from the surface of the brain Nat. Neurosci 18 310–5 [PubMed: 25531570]

[9]. Arzimanoglou A and Kahane P 2008 Textbook of Epilepsy Surgery 1 editor, Luders H The Ictal Onset Zone: General Principles, Pitfalls and Caveats (London: CRC Press) ch 67 pp 595–602 (https://www.taylorfrancis.com/books/edit/10.3109/9780203091708/textbook-epilepsy-surgery-hansluders)

[10]. Basu I, Kudela P, Korzeniewska A, Franaszczuk PJ and Anderson WS 2015 A study of the dynamics of seizure propagation across micro domains in the vicinity of the seizure onset zone J. Neural. Eng 12 046016

[11]. Kellis S, Sorensen L, Darvas F, Sayres C, O'Neill K, Brown RB, House P, Ojemann J and Greger B 2016 Multi-scale analysis of neural activity in humans: implications for micro-scale electrocorticography Clin. Neurophysiol 127 591–601 [PubMed: 26138146]

[12]. Staba RJ, Stead M and Worrell GA 2014 Electrophysiological biomarkers of epilepsy Neurotherapeutics 11 334–46 [PubMed: 24519238]

[13]. Stead M, Bower M, Brinkmann BH, Lee K, Marsh WR, Meyer F B, Litt B, van Gompel J and Worrell GA 2010 Microseizures and the spatiotemporal scales of human partial epilepsy Brain 133 2789–97 [PubMed: 20685804]

[14]. Ray S, Crone NE, Niebur E, Franaszczuk PJ and Hsiao SS 2008 Neural correlates of high-gamma oscillations (60–200 Hz) in macaque local field potentials and their potential implications in electrocorticography J. Neurosci 28 11526–36 [PubMed: 18987189]

[15]. Worrell GA, Gardner AB, Stead SM, Hu S, Goerss S, Cascino GJ, Meyer FB, Marsh R and Litt B 2008 High-frequency oscillations in human temporal lobe: simultaneous microwire and clinical macroelectrode recordings Brain 131 928–37 [PubMed: 18263625]

[16]. Le Van Quyen M, Staba R, Bragin A, Dickson C, Valderrama M, Fried I and Engel J 2010 Large-scale microelectrode recordings of high-frequency gamma oscillations in human cortex during sleep J. Neurosci 30 7770–82 [PubMed: 20534826]

[17]. Schevon CA, Trevelyan AJ, Schroeder CE, Goodman RR, McKhann G and Emerson RG 2009 Spatial characterization of interictal high frequency oscillations in epileptic neocortex Brain 132 3047–59 [PubMed: 19745024]

[18]. Dudek FE 2009 Microseizures in human neocortex: a role for ultra-small seizures? Epilepsy Curr. 9 151–2 [PubMed: 19826511]

[19]. Schevon CA, Ng SK, Cappell J, Goodman RR, McKhann G, Waziri A, Branner A, Sosunov A, Schroeder CE and Emerson RG 2008 Microphysiology of epileptiform activity in human neocortex J. Clin. Neurophysiol 25 321–30 [PubMed: 18997628]

[20]. Osorio I and Frei M 2010 Feasibility of automated warning in subjects with localization-related epilepsies Epilepsy Behav. 19 602–7 [PubMed: 21030315]

[21]. Cook MJ et al. 2013 Prediction of seizure likelihood with a long-term, implanted seizure advisory system in patients with drug-resistant epilepsy: a first-in-man study Lancet Neurol. 12 563–71 [PubMed: 23642342]

[22]. Muller L, Hamilton LS, Edwards E, Bouchard KE and Chang EF 2016 Spatial resolution dependence on spectral frequency in human speech cortex electrocorticography J. Neural. Eng 13 056013

[23]. Wang W et al. 2009 Human motor cortical activity recorded with Micro-ECoG electrodes, during individual finger movements Proc 31st Annu Int Conf IEEE Eng Med Biol Soc Eng Futur Biomed EMBC 2009 pp 586–9

[24]. Leuthardt EC, Schalk G, Roland J, Rouse A and Moran D W 2009 Evolution of brain-computer interfaces: going beyond classic motor physiology Neurosurg. Focus 27 E4

[25]. Rouse AG, Williams JJ, Wheeler JJ and Moran DW 2016 Spatial co-adaptation of cortical control columns in a micro-ECoG brain–computer interface J. Neural. Eng 13 056018

[26]. Flint RD, Rosenow JM, Tate MC and Slutzky MW 2017 Continuous decoding of human grasp kinematics using epidural and subdural signals J. Neural. Eng 14 1–11

[27]. Stacey WC, Kellis S, Greger B, Butson CR, Patel PR, Assaf T, Mihaylova T and Glynn S 2013 Potential for unreliable interpretation of EEG recorded with microelectrodes Epilepsia 54 1391–401 [PubMed: 23647099]

[28]. American Electroencephalographic Society 1994 Guideline twelve: guidelines for long-term monitoring for epilepsy J. Clin. Neurophysiol 11 88–110 [PubMed: 8195430]

[29]. Stacey WC, Kellis S, Patel PR, Greger B and Butson CR 2012 Signal distortion from microelectrodes in clinical EEG acquisition systems J. Neural. Eng 9 56007

[30]. Ad-Tech Medical Instrument Corporation. 2008 Epilepsy and neurosurgery product guide.

[31]. PMT Corporation. 2011 CORTAC® GRIDS & STRIPS 2011.

[32]. Woods V, Trumpis M, Bent B, Palopoli-Trojani K, Chiang C H, Wang C, Yu C, Insanally MNM, Froemke RC and Viventi J 2018 Long-term recording reliability of liquid crystal polymer μ ECoG arrays J. Neural. Eng 15 066024

[33]. Orsborn AL, Wang C, Chiang K, Maharbiz MM, Viventi J and Pesaran B 2015 Semi-chronic chamber system for simultaneous subdural electrocorticography, local field potentials, and spike recordings 2015 7th Int IEEE/EMBS Conf Neural Eng. 2015 pp 398–401

[34]. Jeong J, Hyun Bae S, Seo JM, Chung H and June Kim S 2016 Long-term evaluation of a liquid crystal polymer (LCP)-based retinal prosthesis J. Neural. Eng 13 025004

[35]. Culbertson EC 1995 New laminate material for high performance PCBs: liquid crystal polymer copper clad films Proc—Electron Components Technol Conf. 1995 pp 520–3

[36]. Palopoli-trojani K, Woods V, Chiang C H C, Trumpis M and Viventi J 2016 In vitro assessment of long-term reliability of low-cost μECoG arrays 2016 38th Annu Int Conf IEEE Eng Med Biol Soc. pp 4503–6

[37]. Woodward B 2012 Palladium in temporary and permanently implantable medical devices Platin. Met. Rev 56 213–7

[38]. Schulze D, Tolke R and Widmann I 2014 Noble metal PCB manufacturing for direct implants pcb Mag. (https://iconnect007.com/mags/pdf.php?id=155)

[39]. Bae SH et al. 2012 In vitro biocompatibility of various polymer-based microelectrode arrays for retinal prosthesis Investigative Opthalmol. Visual Sci 53 2653–7

[40]. Micro Systems Technologies DYCONEX AG. dyconex liquid crystal polymer (lcp) substrate proves cytotoxicity conformity according to iso 10993–5

[41]. Petrossians A, Whalen J J, Weiland J D and Mansfeld F 2011 Surface modification of neural stimulating/recording electrodes with high surface area platinum-iridium alloy coatings Proc Annu Int Conf IEEE Eng Med Biol Soc EMBS 2011 pp 3001–4

[42]. Petrossians A, Davuluri N, Whalen JJ, Mansfeld F and Weiland JD 2014 Improved biphasic pulsing power efficiency with Pt-Ir coated microelectrodes MRS Proc. 1621: mrsf13–1621-j07–03 1621 249–57

[43]. Cassar IR, Yu C, Sambangi J, Lee CD, Whalen JJ, Petrossians A and Grill WM 2019 Electrodeposited platinum-iridium coating improves in vivo recording performance of chronically implanted microelectrode arrays Biomaterials 205 120–32 [PubMed: 30925400]

[44]. Wagoner T 2017 Samtec ZA8 Extended Life Test Report 2017 (10.1111/jtxs.12298)

[45]. Arieli A, Grinvald A and Slovin H 2002 Dural substitute for long-term imaging of cortical activity in behaving monkeys and its clinical implications J. Neurosci. Methods 114 119–33 [PubMed: 11856563]

[46]. Ruiz O, Lustig BR, Nassi JJ, Cetin A, Reynolds JH, Albright TD, Callaway EM, Stoner GR and Roe AW 2013 Optogenetics through windows on the brain in the nonhuman primate J. Neurophysiol 110 1455–67 [PubMed: 23761700]

[47]. Chiang CH, Lee J, Wang C, Williams AJ, Lucas TH, Cohen YE and Viventi J 2020 A modular high-density μ ECoG system on macaque vlPFC for auditory cognitive decoding J. Neural. Eng 17 046008

[48]. Witham NS et al. Flexural bending to approximate cortical forces exerted by electrocoticography (ECoG) arrays Prep. (10.1088/1741-2552/ac02dc)

[49]. Trumpis M, Chiang CH, Orsborn AL, Bent B, Li J, Rogers JA, Pesaran B, Cogan G and Viventi J 2020 Sufficient sampling for kriging prediction of cortical potential in rat, monkey, and human μECoG J. Neural Eng 18 036011

[50]. Cogan GB, Iyer A, Melloni L, Thesen T, Friedman D, Doyle W, Devinsky O and Pesaran B 2017 Manipulating stored phonological input during verbal working memory Nat. Neurosci 20 279–86 [PubMed: 27941789]

[51]. Canolty RT, Edwards E, Dalal SS, Soltani M, Nagarajan SS, Kirsch HE, Berger MS, Barbaro NM and Knight RT 2006 High gamma power is phase-locked to theta oscillations in human neocortex Source Sci. New Ser 313 1626–8

[52]. Miller KJ, Zanos S, Fetz EE, Den Nijs M and Ojemann JG 2009 Decoupling the cortical power spectrum reveals real-time representation of individual finger movements in humans J. Neurosci 29 3132–7 [PubMed: 19279250]

[53]. Crone NE, Boatman D, Gordon B and Hao L 2001 Induced electrocorticographic gamma activity during auditory perception Clin. Neurophysiol 112 565–82 [PubMed: 11275528]

[54]. Akbari H, Khalighinejad B, Herrero J, Mehta A and Mesgarani N 2019 Towards reconstructing intelligible speech from the human auditory cortex Sci. Rep 9 874 [PubMed: 30696881]

[55]. Cogan GB, Thesen T, Carlson C, Doyle W, Devinsky O and Pesaran B 2014 Sensory–motor transformations for speech occur bilaterally Nature 507 94–98 [PubMed: 24429520]

[56]. Benjamini Y and Hochberg Y 1995 Controlling the false discovery rate: a practical and powerful approach to multiple testing J. R. Stat. Soc. B 57 289–300

[57]. Insanally M, Trumpis M, Wang C, Chiang C-H, Woods V, Palopoli-Trojani K, Bossi S, Froemke RC and Viventi J 2016 A low-cost, multiplexed μ ECoG system for high-density recordings in freely moving rodents J. Neural. Eng 13 026030

[58]. Duraivel S, Rao AT, Lu CW, Bentley JN, Stacey WC, Chestek CA and Patil PG 2020 Comparison of signal decomposition techniques for analysis of human cortical signals J. Neural. Eng 17 056014

[59]. Cogan SF, Ludwig KA, Welle CG and Takmakov P 2016 Tissue damage thresholds during therapeutic electrical stimulation J. Neural. Eng 13 021001

[60]. Takemi M, Castagnola E, Ansaldo A, Ricci D, Fadiga L, Taoka M, Iriki A and Ushiba J 2017 Rapid identification of cortical motor areas in rodents by high-frequency automatic cortical stimulation and novel motor threshold algorithm Front. Neurosci 11 580 [PubMed: 29089866]

[61]. Lu Y, Lyu H, Richardson AG, Lucas TH and Kuzum D 2016 Flexible neural electrode array based-on porous graphene for cortical microstimulation and sensing Sci. Rep 6 1–9 [PubMed: 28442746]

[62]. Vaskov AK, Irwin ZT, Nason SR, Vu PP, Nu CS, Bullard AJ, Hill M, North N, Patil PG and Chestek CA 2018 Cortical decoding of individual finger group motions using ReFIT kalman filter Front. Neurosci 12 751 [PubMed: 30455621]

[63]. Tandon N, Tong BA, Friedman ER, Johnson JA, Von Allmen G, Thomas MS, Hope OA, Kalamangalam GP, Slater JD and Thompson SA 2019 Analysis of morbidity and outcomes associated with use of subdural grids vs stereoelectroencephalography in patients with intractable epilepsy JAMA Neurol. 76 672 [PubMed: 30830149]

[64]. Pothof F, Bonini L, Lanzilotto M, Livi A, Fogassi L, Orban GA, Paul O and Ruther P 2016 Chronic neural probe for simultaneous recording of single-unit, multi-unit, and local field potential activity from multiple brain sites J. Neural. Eng 13 046006

[65]. Cressie N 1990 The origins of kriging Math. Geol 22 239–52

[66]. Musk E 2019 An integrated brain-machine interface platform with thousands of channels J. Med. Internet Res21 e16194

[67]. Jun JJ et al. 2017 Fully integrated silicon probes for high-density recording of neural activity Nature 551 232–6 [PubMed: 29120427]

[68]. Chiang CH et al. 2020 Development of a neural interface for high-definition, long-term recording in rodents and nonhuman primates Sci. Transl. Med 12 eaay4682

[69]. Worrell GA, Jerbi K, Kobayashi K, Lina JM, Zelmann R and Le Van Quyen M 2012 Recording and analysis techniques for high-frequency oscillations Prog. Neurobiol 98 265–78 [PubMed: 22420981]

[70]. Wiebe S, Blume WT, Girvin JP and Eliasziw M 2001 A randomized, controlled trial of surgery for temporal-lobe epilepsy New Engl. J. Med 345 311–8 [PubMed: 11484687]

[71]. Wetjen NM, Marsh WR, Meyer FB, Cascino GD, So E, Britton JW, Stead S M and Worrell GA 2009 Intracranial electroencephalography seizure onset patterns and surgical outcomes in nonlesional extratemporal epilepsy J. Neurosurg 110 1147–52 [PubMed: 19072306]

[72]. Blanco JA et al. 2011 Data mining neocortical high-frequency oscillations in epilepsy and controls Brain 134 2948–59 [PubMed: 21903727]

[73]. Tarulli A, Devinsky O and Alper K 2001 Progression of postictal to interictal psychosis Epilepsia 42 1468–71 [PubMed: 11879351]

[74]. Beauchamp MS, Oswalt D, Sun P, Foster BL, Magnotti JF, Niketeghad S, Pouratian N, Bosking WH and Yoshor D 2020 Dynamic stimulation of visual cortex produces form vision in sighted and blind humans Cell 181 774–783.e5 [PubMed: 32413298]

[75]. Miller KJ, Leuthardt EC, Schalk G, Rao RPN, Anderson NR, Moran DW, Miller J W and Ojemann J G 2007 Spectral changes in cortical surface potentials during motor movement J. Neurosci 27 2424–32 [PubMed: 17329441]

[76]. Mehring C, Rickert J, Vaadia E, Cardosa De Oliveira S, Aertsen A and Rotter S 2003 Inference of hand movements from local field potentials in monkey motor cortex Nat. Neurosci 6 1253–4 [PubMed: 14634657]

[77]. Thongpang S et al. 2011 A micro-electrocorticography platform and deployment strategies for chronic BCI applications Clin. EEG Neurosci 42 259–65 [PubMed: 22208124]

[78]. Kellis S, Miller K, Thomson K, Brown R, House P and Greger B 2010 Decoding spoken words using local field potentials recorded from the cortical surface J. Neural. Eng 7 056007

[79]. Kellis SS, House PA, Thomson KE, Brown R and Greger B 2009 Human neocortical electrical activity recorded on nonpenetrating microwire arrays: applicability for neuroprostheses Neurosurg. Focus 27 E9

[80]. Middlebrooks JC, Bierer JA and Snyder RL 2005 Cochlear implants: the view from the brain Curr. Opin. Neurobiol 15 488–93 [PubMed: 16009544]

[81]. Froemke RC, Heman-Ackah S and Waltzman S 2014 Cochlear Implant 3rd edn editors Waltzman S and Roland JT Auditory Neuroplasticity (Thieme) 4 38–46

[82]. Rao VR, Sellers KK, Wallace DL, Lee MB, Bijanzadeh M, Sani OG, Yang Y, Shanechi MM, Dawes HE and Chang EF 2018 Direct electrical stimulation of lateral orbitofrontal cortex acutely improves mood in individuals with symptoms of depression Curr. Biol. 28 3893–3902.e4

[83]. Sani OG, Yang Y, Lee MB, Dawes HE, Chang EF and Shanechi MM 2018 Mood variations decoded from multi-site intracranial human brain activity Nat. Biotechnol 36 954

[84]. Milekovic T et al. 2018 Stable long-term BCI-enabled communication in ALS and locked-in syndrome using LFP signals J. Neurophysiol 120 343–60 [PubMed: 29694279]

[85]. Baud MO, Kleen JK, Anumanchipalli GK, Hamilton LS, Tan YL, Knowlton R and Chang EF 2018 Unsupervised learning of spatiotemporal interictal discharges in focal epilepsy Neurosurgery 83 683–91 [PubMed: 29040672]

[86]. Gliske SV, Irwin ZT, Chestek C, Hegeman GL, Brinkmann B, Sagher O, Garton HJL, Worrell GA and Stacey WC 2018 Variability in the location of high frequency oscillations during prolonged intracranial EEG recordings Nat. Commun 9 2155 [PubMed: 29858570]

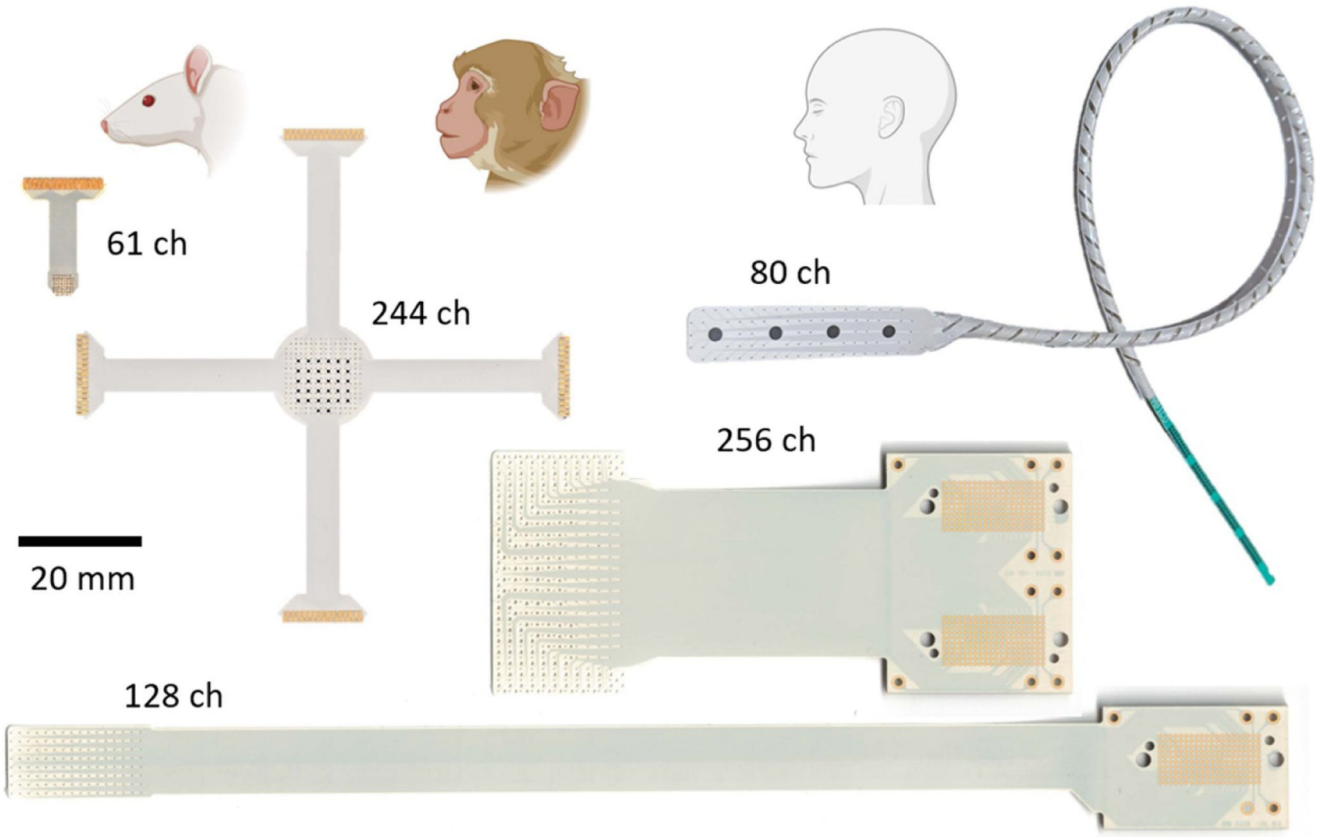

Electrode Array Specifications

Electrode (# Ch)	Contact size (mm, Dia.)	Spacing (mm)	Coverage (mm^2)	Density (Ch. / mm^2)	Purpose
61	0.23	0.42	3.4 x 3.4	5.96	Rodent
244	0.20	0.76	12 x 12	1.64	NHP and human
256	0.20	1.72	38 x 21	0.33	Human intraoperative
128	0.20	1.33	11 x 21	0.56	Human intraoperative
80 — 4x macro	2.30	10	10 x 40	0.20	Human short-term implantation
80 — 76x micro	0.20	2			

Figure 1.

Five liquid crystal polymer (LCP) thin-film (TF) electrode designs with varied coverage and high-density electrode spacing designed for use in rodents, non-human primates (NHP) and humans. (Top) Photos of electrode arrays. The 61 and 244ch arrays use zero insertion force (ZIF) connectors and the 80, 128, and 256ch arrays use ultra-low profile, high-density (0.8 mm pitch) spring connectors. Both connector designs do not require soldering or post-manufacturing assembly. The 80ch electrode array incorporates a hybrid design with four clinical standard macroelectrodes interspersed with 76 microelectrodes. (Bottom) Table

of electrode specifications. The same LCP-TF manufacturing process can be used to simultaneously fabricate large and small electrode array designs.

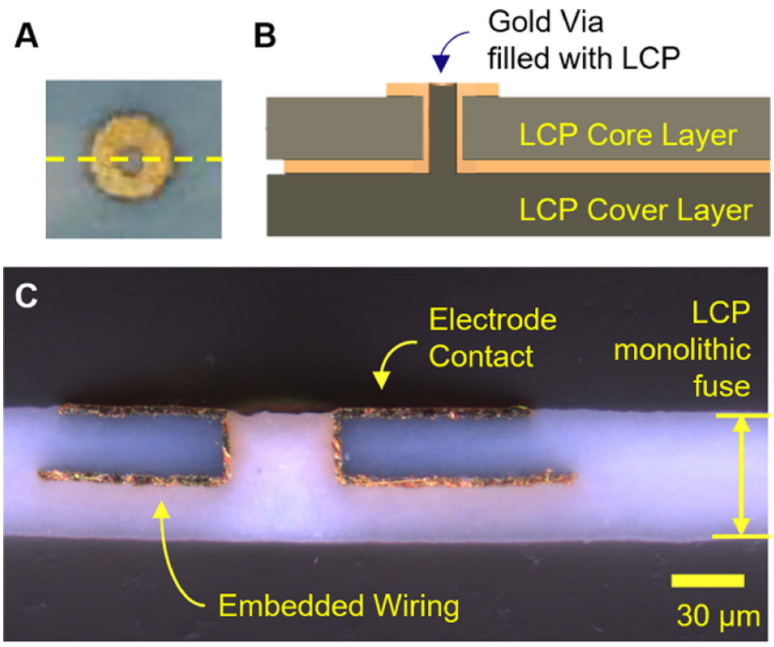

Figure 2.

Electrode cross section. (A) Photo of an electrode contact on a 61ch array. The yellow dashed line indicates the cross-section shown in (B) and (C). (B) Illustration of the electrode array layer stack-up. The electrode array wiring was embedded between the the LCP core and cover layers. The electrode contacts were flush with or slightly protruded from the surface of the LCP substrate. (C) Microscope photo of an example LCP-TF electrode array cross-section showing embedded wiring and an electrode contact. Two LCP sheets were thermally fused to form a single uniform LCP layer without a distinguishable border or fusion point.

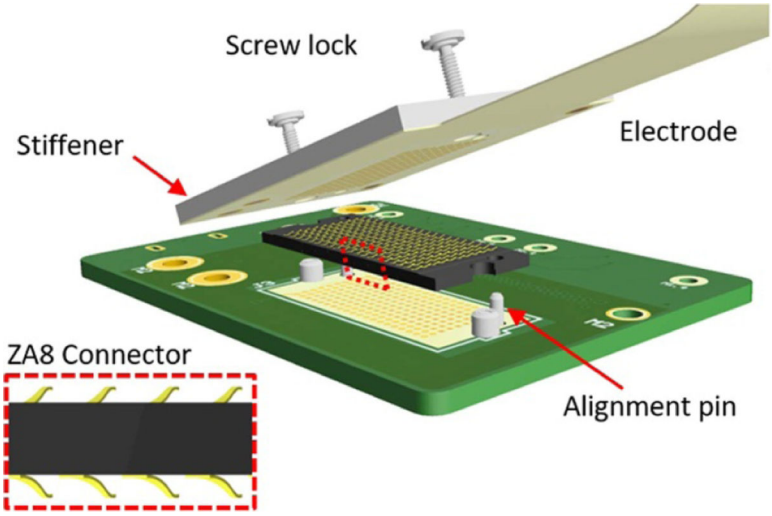

Figure 3.

3D illustration of the ultra-low profile, high-density (0.8 mm pitch) spring connector. The LCP-TF electrode array design included four alignment holes and a stiffener to increase the thickness and rigidity of the device in the connector area. The alignment holes and stiffener were standard features of the LCP flexible circuit process. (Inset) A side view of the spring connector highlighting the metal springs on the top and bottom of the connector.

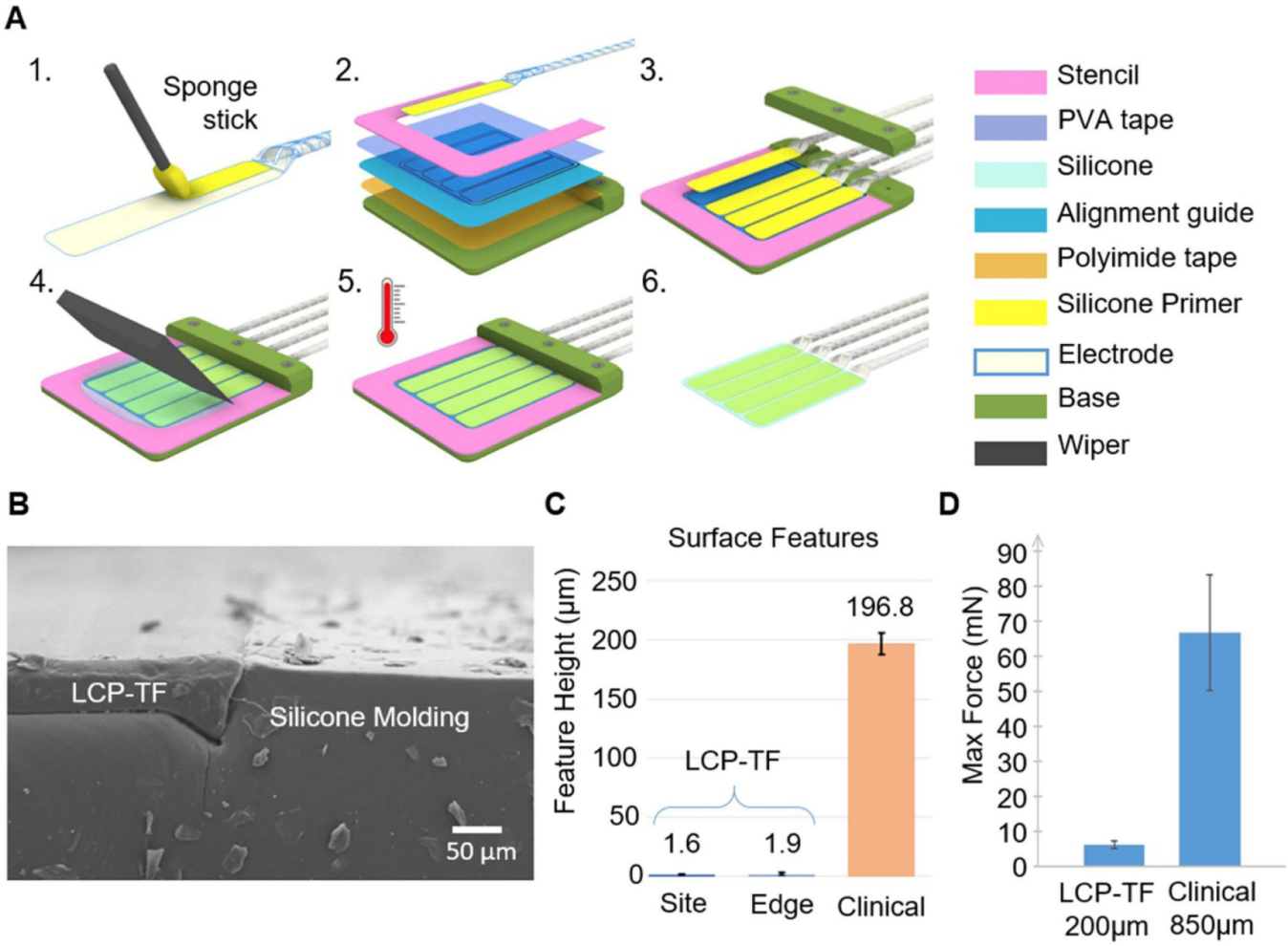

Figure 4.

Silicone electrode array molding procedure to combine multiple LCP-TF arrays together and provide soft edges to prevent damage to the cortex. (**A**) Illustrations of the electrode molding process. 1. Silicone primer was applied on the back side of the electrode and dried at room temperature for 30 min. 2. Double-sided polyimide tape was used to hold the alignment guide to the molding base. Double-sided transparent water soluble tape (PVA) was attached to the mold and the LCP-TF array to prevent silicone from covering the electrode contacts. A stencil was used to determine the shape and thickness of the silicone mold. 3. The LCP-TF array(s) were aligned and laminated onto the PVA tape using the alignment guide. 4. Well-mixed and degassed silicone was poured onto the mold. A wiper used to remove excessive silicone. 5. The silicone was cured at 60 °C for 2 h. 6. The assembly was soaked and rinsed with warm (>40 °C) DI water to remove the PVA tape and release the molded array. (**B**) SEM image of the cross section of a molded array showing the flat surface at the transition from the LCP-TF to silicone. Dust on the surface and side of the array were generated from the cross-sectional cut and not present normally. (**C**) Profilometer measurements of the electrode contact step height (Site) and the surface of the LCP-TF to silicone transition (Edge) showed a much flatter surface profile than conventional subdural clinical electrodes. (**D**) The LCP-TF prototype device was ~11× less

stiff than the commercial ECoG array. Maximum possible bending force that could be exerted on the brain derived from four-point bending tests and an analysis of brain geometry. A commercially available electrode array as well as an LCP-TF device prototype without Au traces were measured. The error bars indicate a standard error of means for all bending angles tested. The mean and SEM force for the LCP-TF prototype device was 6 ± 1 mN, while the commercial ECoG array force was 67 ± 17 mN.

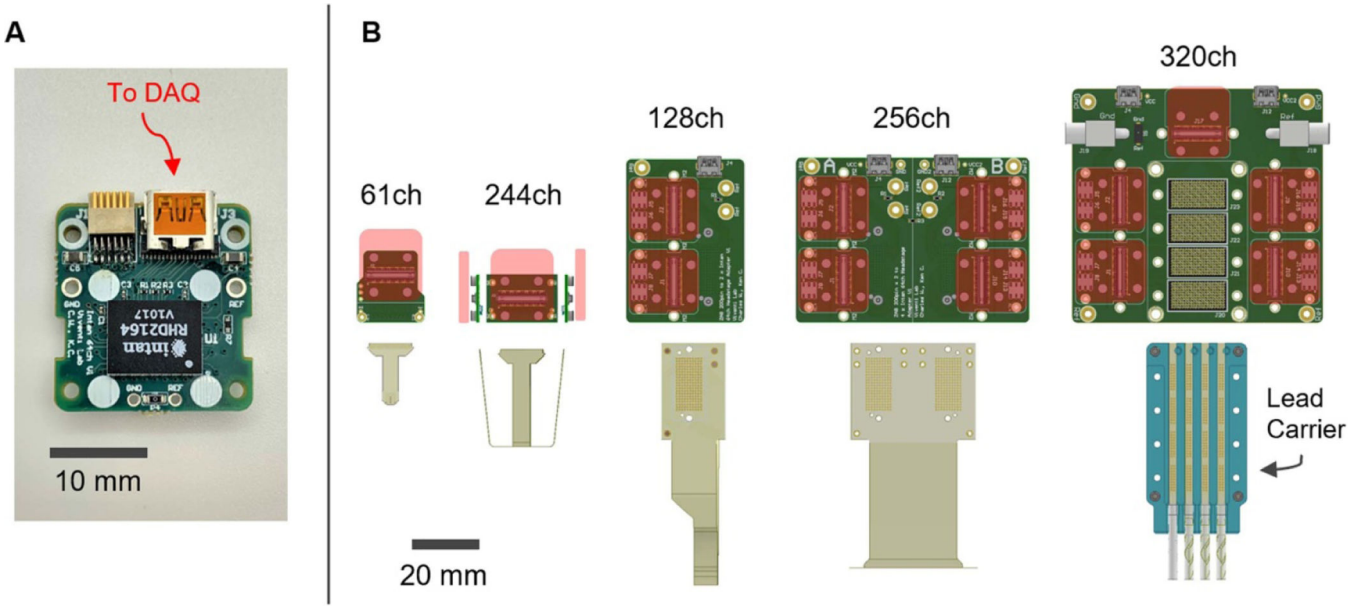

Figure 5.

Modular data acquisition system. (A) Photograph of custom digitizing headstage utilizing the Intan RHD2164 chip. This headstage can be connected through commonly used Omnetics connector or a standard micro-HDMI cable. (B) Modular adapter boards were fabricated to attach the digitizing headstage to the five different LCP-TF electrode designs. Red rectangles denote the position and the size of the digitizing headstage when connected. The 320ch system is designed for short-term implantation that uses 4× 80ch arrays to cover 4×4 cm^2 of the cortex.

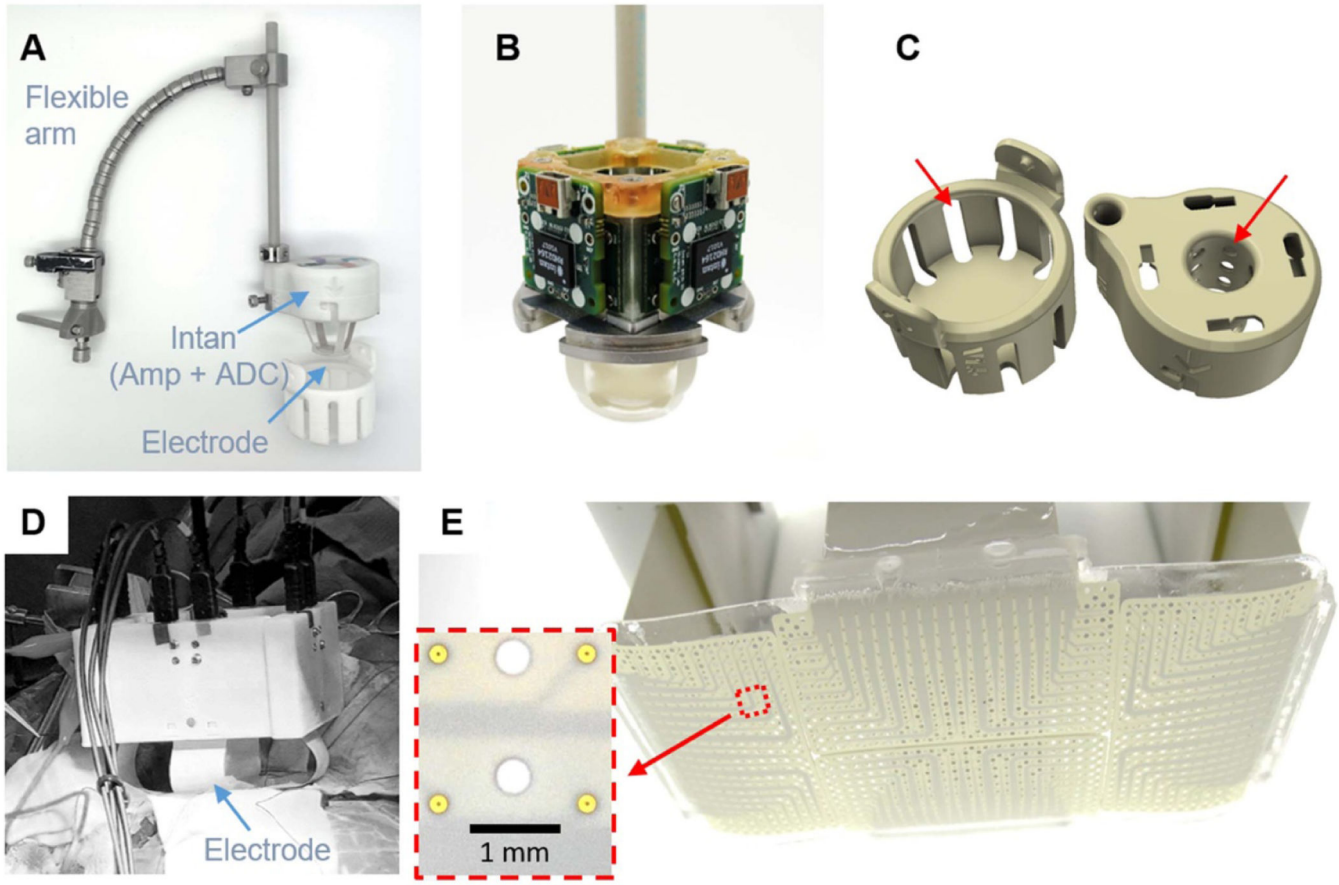

Figure 6.

Intraoperative recording setup for open craniotomy procedures. (A) A flexible arm was used to hold the 244ch setup on top the craniotomy. Custom digitizing headstages were attached to the LCP-TF array and mounted to a metal base inside the 3D printed cap. The headstages were located as close as possible to the electrode array to reduce the effect of environmental noise sources. (B) Modular adapter PCBs were secured to the metal frame with screws. The metal base was also used to share the ground and reference among the four digitizing headstages. (C) 3D printed cases were used to protect the electrode and electronics during sterilization and handing. Slot openings (red arrows) were added to ensure the sterilization gas reached every component. (D) The recording setup can be scaled up to 1024ch. (E) The 1024ch electrode consisted of four 256ch array molded together to cover a 4×8 cm^2 cortical area. The inset shows detail of the electrode contacts, which were 200 μm in diameter and spaced 1.7 mm apart. Holes were added wherever possible to the design to increase flexibility.

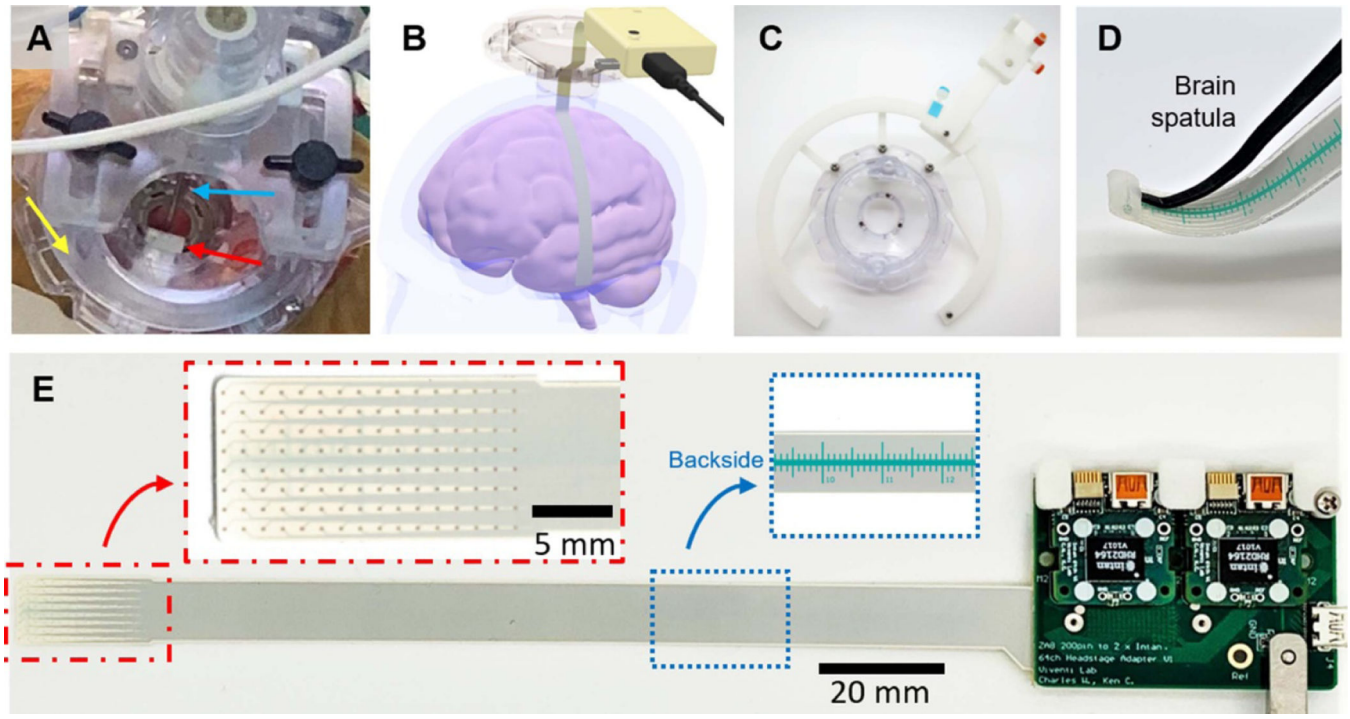

Figure 7.

Intraoperative recording setup for experimental access through a burr hole. (A) Photograph of the experiment. An LCP-TF electrode (red arrow) was inserted through burr hole during a deep brain stimulation (DBS) surgery. The DBS base (Nexframe, yellow arrow) and lead (blue arrow) were used without any obstruction. (B) 3D rendering illustrates that the electrode was advanced under the dura more than 80 mm away from the burr hole, reaching the temporal lobe during a language study. (C) A custom 3D printed track system helped to hold the electronics at any angle from the implant site. (D) A pocket was molded at the tip of the electrode array to allowing a malleable brain retractor (brain spatula) to be used as an insertion tool to guide the electrode placement. (E) Photograph of the assembled LCP-TF array and recording system. Two digitizing headstages were connected to the modular adaptor board, requiring only a single μHDMI cable to be connected to the recording controller. Red inset shows the detailed view of the 128 electrode contacts. Blue inset shows the ruler, printed with biocompatible soldermask, on the back side of the LCP-TF electrode. The ruler was used to provide the surgeon relative position information while advancing the array under the dura.

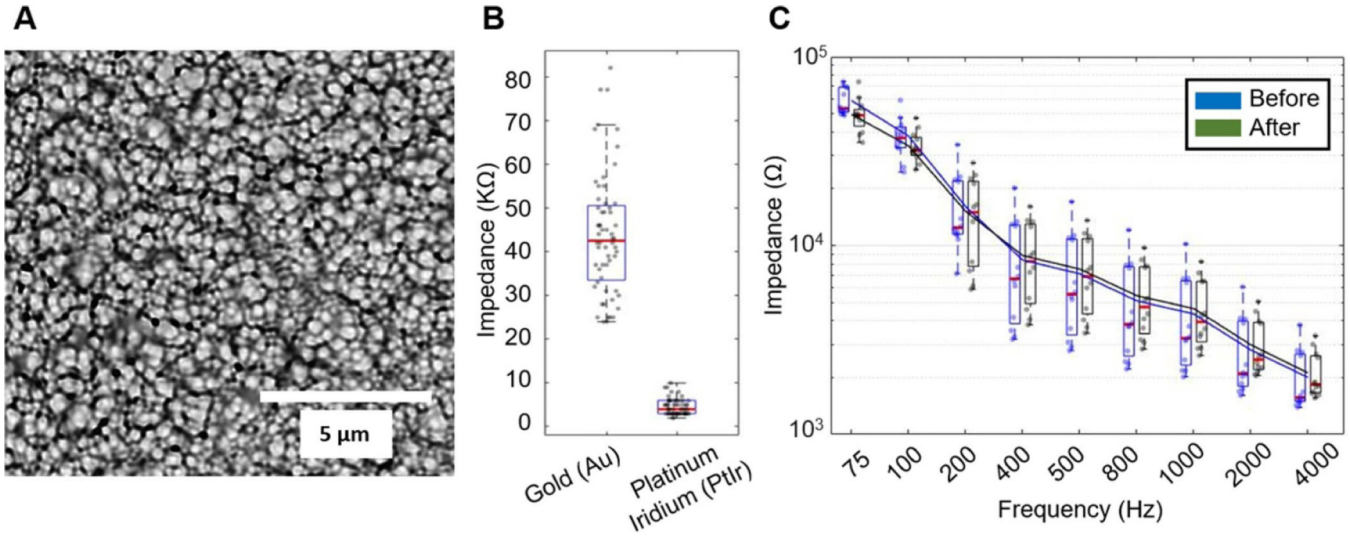

Figure 8.

LCP-TF electrodes were electroplated with platinum iridium (PtIr) to reduce electrode impedance and enable stimulation. (A) SEM picture of the PtIr-plated electrode surface. (B) Impedance measurement comparing gold electrodes (44 ± 13.9 kΩ) before PtIr coating and after (4.6 ± 1.8 kΩ) at 1 kHz. The red line in the boxplot indicates the median value. All data points are shown as the dots within the box plot ($N = 60$). (C) Electrode impedance spectroscopy (EIS) measurements of 12 electrodes taken before and after 1 M pulses of biphasic stimulation at 100 μs per phase, 124 μA, and 50 Hz repetition rate showed no change in electrode impedance. The lines are the average impedances. No damage to the electrode contacts was observed.

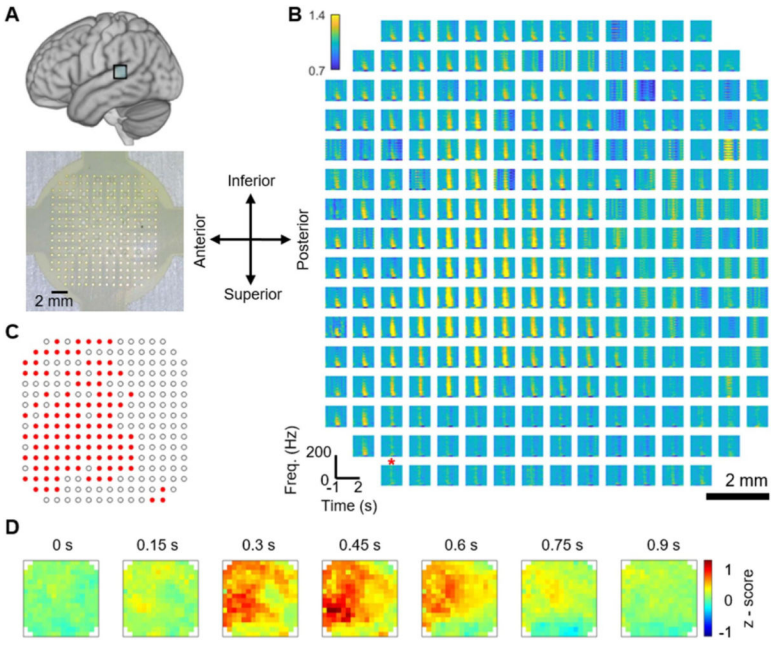

Figure 9.

Example LCP-TF electrode human intraoperative recording to study speech and language. (A) A 244-channel LCP-TF electrode array (bottom) recorded auditory responses from the posterior superior temporal gyrus (pSTG—top) in a patient undergoing treatment for pharmacologically resistant epilepsy. The patient was asleep during the auditory stimulus (words and non-words) presentation. The *in vivo* electrode impedance data can be found in supplemental figure 3. (B) Spectrograms for the local field from each channel (right) show auditory responses on selective channels. These responses were mainly found in the high gamma (HG) frequency range (70–150 Hz), shown to be a correlate of multi-unit neuronal firing. The red star denoted the high impedance channel. (C) The red channels exhibit significant high-gamma responses during auditory onset relative to baseline (one-sided permutation test, $p < 0.05$, FDR corrected). (D) Normalized HG time-series heat maps show the spatial detail of the auditory response.

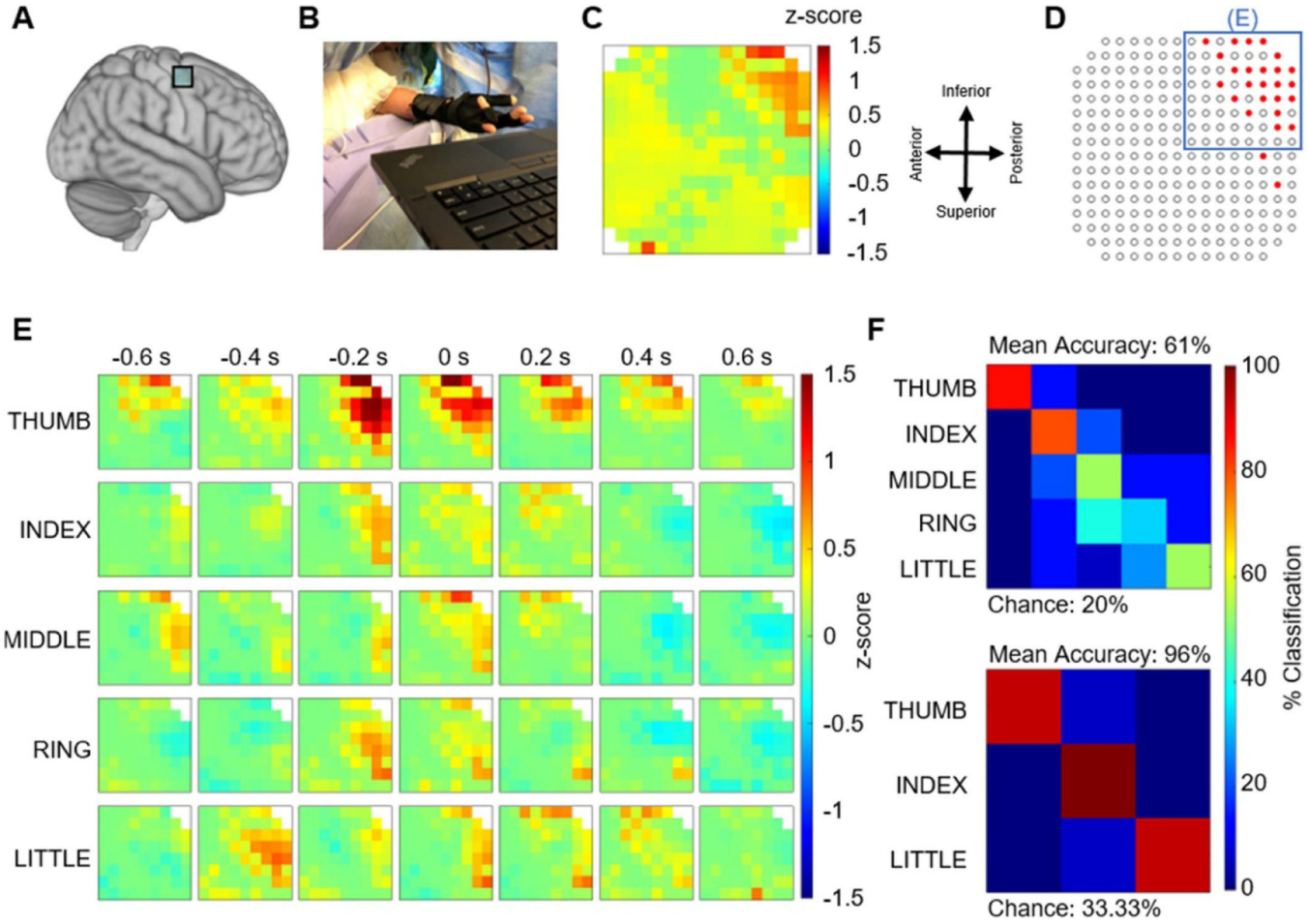

Figure 10.

Example LCP-TF electrode human intraoperative recording to study motor responses. (A) A 244-ch LCP-TF electrode array recorded neural activity during voluntary finger movement from the 'hand-knob' region of the motor cortex of a patient undergoing tumor resection. The electrode impedance data for this array can be found in supplemental figure 4. (B) The participant performed a finger movement task following visually presented cues. The finger kinematics were recorded using a data glove. (C) Normalized high gamma (HG) responses (70–150 Hz; maximum values from −500 ms to 500 ms at movement onset) revealed spatial features of the finger movements focused on the top right corner of the array. (D) A statistical analysis (one-sided permutation test) was performed to determine the channels with significant HG responses during movement onset relative to baseline ($p <$ 0.05, FDR corrected). The blue box indicates the 8 × 8 area of the array that is the focus for panel E. (E) Spatial maps of normalized high-gamma responses separated by finger types during movement. 0 s indicates the onset of finger movement from the glove data. (F) Finger flexion decoding using a linear classification scheme (leave-one-out cross-validation) obtained 61% and 96% classification accuracies for five-finger and three-finger decoders, respectively.

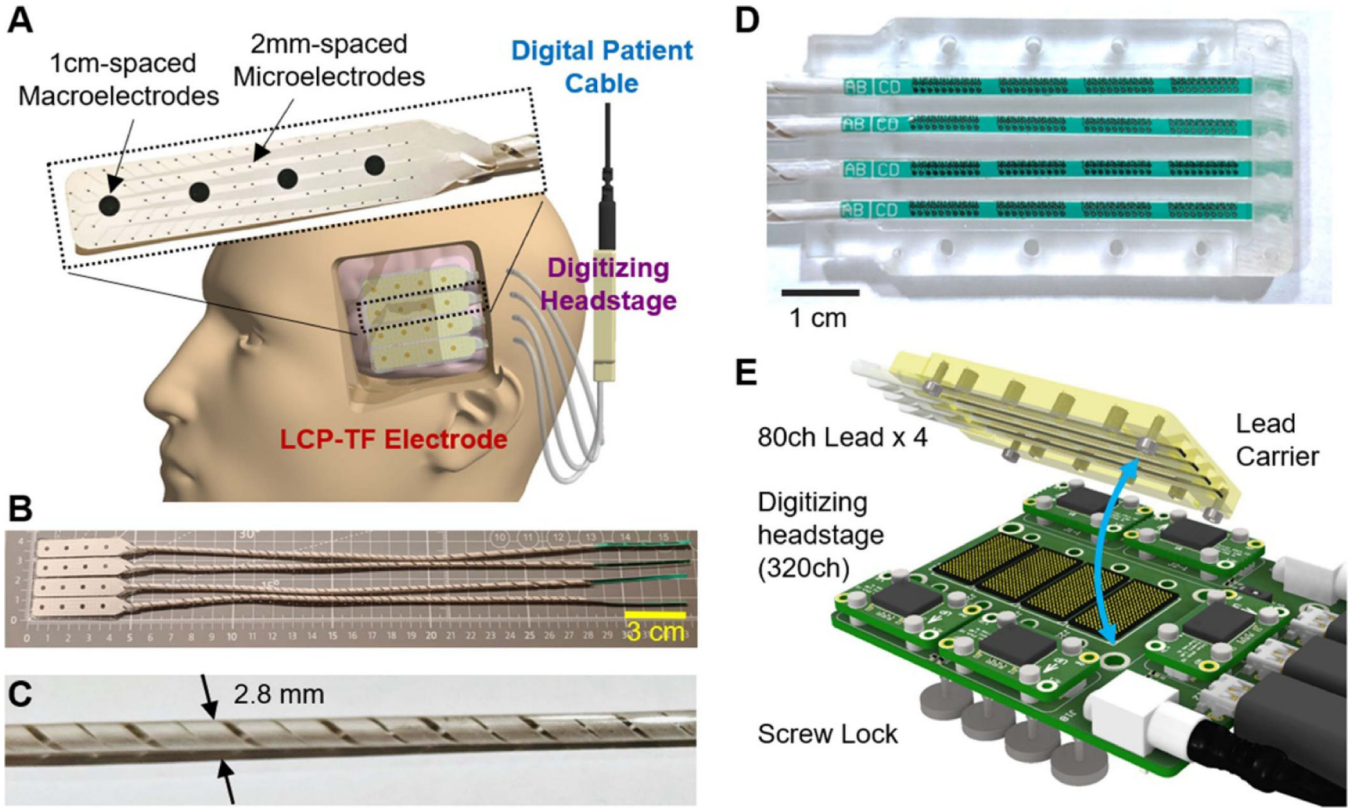

Figure 11.

LCP-TF electrode and recording system design for human short-term implantation. (A) The LCP-TF electrode can be placed through a small craniotomy and advanced under the skull. Our LCP-TF semi-chronic system includes conventional 2.3 mm diameter macroelectrodes spaced 10 mm apart and 200 μm diameter microelectrodes spaced 2 mm apart. Coiled leads were designed to be tunneled out of the scalp using a cannula and connected to the digitizing headstage. The digitizing headstage provides signal amplification and digitization in the patient head bandages. (B) Assembled and molded LCP-TF electrode array with 16 macro- and 304 microcontacts. (C) The coiled leads were molded to a 2.8 mm diameter cable, in order to fit into a standard 3 mm diameter cannula. (D) A custom lead carrier was designed to assist the alignment of the leads to the spring connector. (E) Detailed view of the design of the high-density connector system to the digitizing headstage, showing the connector alignment and connecting mechanism.

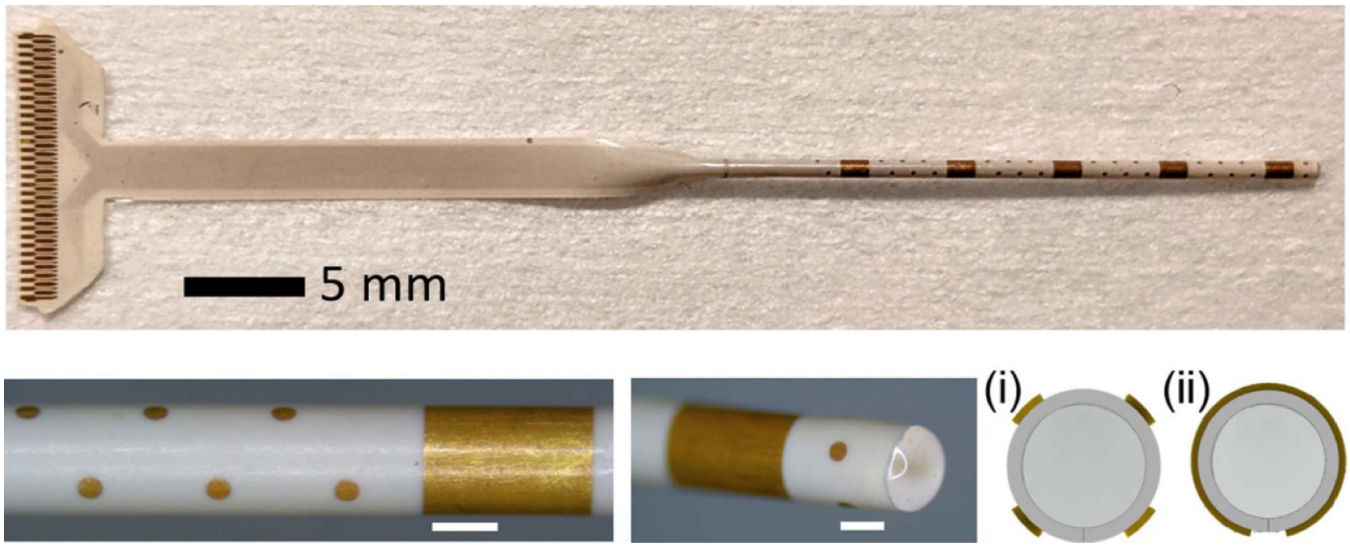

Figure 12.

LCP-TF SEEG prototype includes 56 microelectrodes with 500 μm spacing and five macroelectrodes with 5 mm spacing. The physical form factor is the same as standard clinical SEEG electrodes (900 μm diameter), making it compatible with existing clinical workflows. Cross sectional drawings illustrate the arrangement of four microelectrodes around the circumference of the array (i), while the macroelectrodes wrap around the entire array (ii).